

The supplementary information contains four sections: 1) scaling tidal strain rates and stresses from Europa to Enceladus; 2) calculating the resolved stresses on a fault; 3) details of the shear heating model, including estimates of the minimum shell thickness required; 4) details of the vapour transport model.

1. Scaling from Europa

To obtain an order-of-magnitude estimate (a more precise approach is detailed below) of the characteristic tidal stresses and strain rates present, one can simply scale from previously calculated stresses on Europa, under the assumption of spherically symmetrical satellite properties. Using the expressions given in Murray and Dermott [29] and Ojakangas and Stevenson [30], it may be shown that the ratio of peak diurnal tidal stress on two satellites is given by

$$\frac{\sigma_1}{\sigma_2} = \frac{e_1}{e_2} \frac{h_{21}}{h_{22}} \frac{M_1}{M_2} \frac{m_2}{m_1} \left(\frac{R_1}{R_2} \right)^3 \left(\frac{a_2}{a_1} \right)^3 \quad (1)$$

where e , h_2 , M , m , R and a are the orbital eccentricity, Love number, primary and satellite mass, satellite radius and semi-major axis, respectively. Thus, the ratio of the peak stress on Enceladus to that on Europa is given by $6 (h_{21}/h_{22})$. Peak diurnal tidal stresses in polar regions on Europa are ~ 100 kPa [15] and the value of h_2 for Europa is ≈ 1.25 [16], so peak stresses on Enceladus are $\sim 500 h_2$ kPa.

Assuming an elastic response, the mean strain will scale linearly with the peak stress; the ratio of the mean strain rates requires the inclusion of one extra term in equation (1), the ratio of the two satellite orbital periods (t_2/t_1). For parameters appropriate to Enceladus and Europa, the ratio of the strain rate on Enceladus to that on Europa is $15 (h_{21}/h_{22})$. The mean strain rate on Europa [30] is $2 \times 10^{-10} \text{ s}^{-1}$ and thus the mean strain rate $\dot{\epsilon}$ on Enceladus is $3 \times 10^{-9} h_2 \text{ s}^{-1}$.

Following Greenberg et al. [15, Section III], the local strain on individual cracks depends on the tidal strain and the crack separation d . If the cracks are free to move, then the mean shearing velocity on the cracks is given by $\dot{\epsilon} d$. Because of the combination of compressional normal stresses and friction, the cracks are

likely to be locked for at least half the tidal cycle [13], although we note that such locking is not fundamental to our model. The mean shear velocity is thus unlikely to exceed $4.5 \times 10^{-5} h_2 (d/30 \text{ km}) \text{ ms}^{-1}$.

For the example shown in Fig 1, a shear velocity of $8 \times 10^{-6} \text{ ms}^{-1}$ implies $h_2 \approx 0.2$, for which the peak stress is $\sim 100 \text{ kPa}$. For a coefficient of friction $f=0.3$, this stress is sufficient to cause shear motion to 3.4 km depth, comparable to the 4 km depth obtained by the model.

2. Resolving tidal stresses onto fractures

The above arguments are sufficient to predict the general amplitude of diurnal tidal stresses. However, to calculate the stresses resolved on an individual fault segment requires a more exact approach. Here we adopt the approach using the methods outlined in Mullen et al. [31] and Wahr [32]. These methods allow the radial, tangential and shear components of the tidal stress to be calculated as described below.

Define $z = 3 GMR^2 / 2a^3$ where M is the primary mass, R is the satellite radius, a is its semi-major axis and G is the gravitational constant. Also define $\Delta = (3\lambda + 2\mu) / (\lambda + 2\mu)$ where λ and μ are the Lamé parameters, $c_1 = z\mu/gR$ where g is the acceleration at the surface of the satellite, and $c_2 = h_2 - 3l_2$ where h_2 and l_2 are degree-two Love numbers. The diurnal radial ($\sigma_{\theta\theta}$), tangential ($\sigma_{\phi\phi}$) and shear ($\sigma_{\theta\phi}$) stresses are given by:

$$\sigma_{\theta\theta} = c_1 e \left\{ -\cos m \left[3l_2 \sin^2 \theta + c_2 \Delta (3 \cos^2 \theta - 1) \right] + \frac{1}{2} \left[l_2 (1 + \cos^2 \theta) + c_2 \Delta \sin^2 \theta \right] \left[-\cos(2\phi + m) + 7 \cos(2\phi - m) \right] \right\}$$

$$\sigma_{\phi\phi} = c_1 e \left\{ -\cos m \left[-3l_2 \sin^2 \theta + c_2 \Delta (3 \cos^2 \theta - 1) \right] + \frac{1}{2} \left[-l_2 (1 + \cos^2 \theta) + c_2 \Delta \sin^2 \theta \right] \left[-\cos(2\phi + m) + 7 \cos(2\phi - m) \right] \right\}$$

$$\sigma_{\theta\phi} = c_1 e l_2 \cos \theta \left[\sin(2\phi + m) - 7 \sin(2\phi - m) \right]$$

Here e is the satellite eccentricity, $m=nt$ is the angular position in the orbit where n =mean motion and t is time, θ and ϕ are the colatitude and longitude of the point in question. We are neglecting non-synchronous rotation and assuming the satellite obliquity is zero. Figure A shows the resulting stresses over one tidal

cycle at a particular point in the southern hemisphere of Enceladus, demonstrating that the peak stresses approach ~ 100 kPa for $h_2=0.2$, as expected.

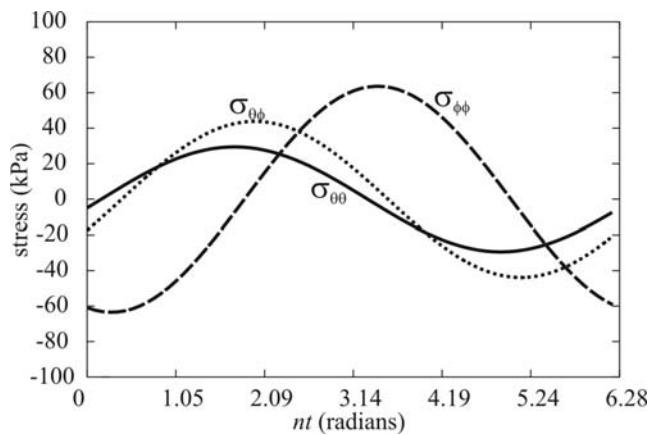


Figure A. Diurnal stress components at 165°W , 70°S for Enceladus. Here n is the mean motion and t is time relative to periapse. We use $h_2=0.2$, $l_2=0.04$, $\mu=3.5$ GPa, $\lambda=6.8$ GPa, $g=0.11\text{ms}^{-2}$, $R=252$ km, $e=0.0047$.

To obtain the resolved stresses, we consider a fault segment located at longitude ϕ , colatitude θ (see Figure B). The tidal radial, tangential and shear stresses at this point $\sigma_{\theta\theta}$, $\sigma_{\phi\phi}$ and $\sigma_{\theta\phi}$ are calculated using the method outlined above.

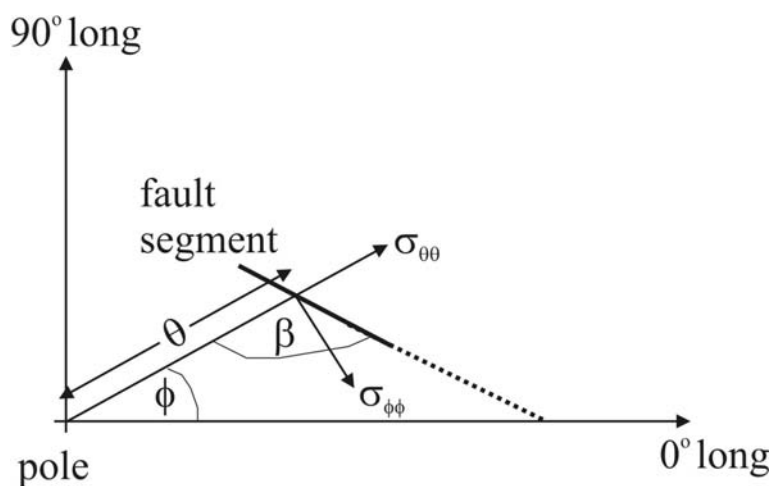


Figure B. Geometry for calculating resolved stresses on a fault segment.

We are interested in the resolved normal and shear stresses $\sigma'_{\theta\theta}$ and $\sigma'_{\theta\phi}$, respectively, on a fault segment which has an orientation β with respect to the radial direction (see Figure B). Following Turcotte and Schubert [33, equations 2-37 and 2-40] and defining $\beta' = \beta - \frac{\pi}{2}$ we obtain

$$\sigma'_{\theta\phi} = \frac{1}{2}(\sigma_{\phi\phi} - \sigma_{\theta\theta})\sin 2\beta' + \sigma_{\theta\phi}\cos 2\beta'$$

$$\sigma'_{\theta\theta} = \sigma_{\theta\theta}\cos^2\beta' + \sigma_{\phi\phi}\sin^2\beta' + \sigma_{\theta\phi}\sin 2\beta'$$

These expressions allow us to calculate the resolved shear stress as a function of time at any point on a fault segment. We expect that the mean shear velocity will scale with the shear stress (Section 1 above – note that here we are neglecting variations in the tiger stripe spacing d ; see also [13]). We therefore calculate the mean absolute shear stress over one tidal cycle as a proxy for the expected mean shear velocity. For frictional heating, the heating rate is proportional to the shear velocity; therefore, the mean absolute shear stress will provide a measure for the relative long-term heating rates on different fault segments.

3. Shear heating model description

The basic model is described in [8] and the modification to self-consistently solve for the brittle layer depth is described in [9]. The vertically integrated heat production per unit length due to fault friction is given by $f\rho gz^2u/2$, where f is the coefficient of friction, g is the acceleration due to gravity, z is the depth of the brittle zone and ρ is the ice density. The model is in steady-state, and thus the initiation of the fault motion is not considered. One possibility is that local viscous dissipation arises, leading to elevated geotherms and a brittle layer that is thin enough to allow tidal stresses to then drive fault motion. The base of the conductive portion of the shell is set at a temperature of 270 K; a reduction in this basal temperature of a few tens of K will occur if the conductive layer is underlain by a convecting layer, but we find that such a change does not have a significant effect on the total vapour production. Because the orbital period of Enceladus (1.37 days) is much shorter than the characteristic heat diffusion timescale, a constant mean shear velocity can be assumed [8].

Three additional model modifications are described here: incorporation of a vapour sublimation term; calculation of the surface temperature in radiative balance; and viscosity variation due to pre-melting.

The modified heat conduction equation to be solved is given by

$$\frac{\partial T}{\partial t} = \kappa \nabla^2 T + \alpha \frac{H}{\rho C_p} \quad (2)$$

where T is temperature, t is time, κ is thermal diffusivity, H is the heating rate (due to brittle or ductile shear) in Wm^{-3} , ρ is the density and C_p the specific heat capacity. Here α is a free parameter ($0 \leq \alpha \leq 1$) which describes how energy is partitioned between heating and vapour production. If $\alpha=1$, all the energy goes into heating, no vapour is produced, and the equation reverts to the form used in [8]. If $\alpha=0$, all the energy goes into vapour production and no heating occurs, resulting in a steady-state linear heat conduction temperature profile. Here we are neglecting other potential sinks of energy (which are expected to be minor), such as mechanical damage and the energy required to create new fault surfaces. Although here we are treating α as a free parameter, in reality it will be governed by the extent to which sublimation causes a local increase in vapour pressure, thereby reducing or eliminating further sublimation. The crucial parameters are thus the timescales of sublimation and gas transport [19]. Modelling these values is beyond the scope of the current work, but laboratory experiments [19] suggest that the gas transport timescale is likely to be rapid, resulting in $\alpha \ll 1$.

The vapour production rate depends on $(1-\alpha)H$, that part of the dissipation not going into heating. The production of vapour ($\alpha < 1$) results in a colder temperature structure, a deeper brittle layer, and thus a greater total amount of dissipation.

In order to calculate the heat production per unit length, we separately consider the contributions from frictional and viscous heating and possible vapour recondensation. The volumetric heating rate which contributes to the change in temperature, αH , is calculated using equations 3 and 5 in [8]. In steady state,

solution of equation (2) and the derivation of the surface temperature (see below) allows the conductive surface heat flux to be calculated. The total conductive heat flow is calculated by integrating the heat flux across the computational domain, and then multiplying by the total tiger stripe length (500 km). Vapour recondensation may occur in the near-surface, in which case latent heat will be given out. The total vapour flux is calculated using the methods described below. Given a vapour flux (in kg/s), the maximum heat flow due to recondensation is calculated by multiplying the vapour flux by the latent heat (assuming a constant value of 2.8 MJ/kg). In practice, some vapour will not recondense, giving rise to the observed plumes.

Surface temperatures T_s in the presence of a subsurface conductive heat flux (Fig. 1) are calculated numerically by solving the following equation, which balances the absorbed and subsurface conductive heat fluxes against the re-radiated heat:

$$\varepsilon\sigma T_s^4 + k \frac{T_s}{\Delta z} = F_{sol} + k \frac{T_2}{\Delta z}$$

Here ε is the emissivity ($=1$), σ is Stefan's constant ($\sigma = 5.7 \times 10^{-8} \text{ W m}^{-2} \text{ K}^{-4}$), k is the thermal conductivity, F_{sol} is the absorbed solar heat flux required to generate an equilibrium temperature of 75K in the absence of subsurface heating, T_2 is the temperature one grid point beneath the surface and Δz ($=0.2 \text{ km}$) is the grid point spacing in the z -direction.

Experimental observations [27] show that the viscosity of ice drops steeply within about 20 K of the melting point. We implemented this effect by defining a dimensionless temperature

$T' = 1 + [(T - T_m) / 20]$ where T_m is the melting temperature (270 K) and multiplying the (temperature-dependent) viscosity by an additional factor F when $T' > 0$, where

$$F = (0.03)^{T'}$$

This approach reduces the viscosity by an additional factor of ~ 30 over the temperature range ($T_m - 20 \text{ K}$) to T_m . In practice, this effect is unimportant because vapour production generally ensures that temperatures do

not approach the melting temperature except towards the base of the ice shell, where heat production is small.

To investigate the effect of shell thickness on heat production, two factors must be taken into account. First, from volumetric considerations total heat production will be reduced as the ice shell thins. Second, however, a thinner ice shell results in greater deformation and shear velocities (Fig. 4). These two factors trade off against each other. We used an assumed viscosity of 10^{13} Pa s to calculate h_2 and hence the shear velocity u for shells of varying thicknesses. For each shell thickness, we then ran a model similar to that shown in Fig. 1 with the appropriate velocity. Figure C shows how the tidal deformation (as measured by h_2) increases with decreasing shell thickness, but that the total heat production peaks at intermediate shell thicknesses because of the trade-off between tidal deformation and volume. Models producing less than 3.9 GW heat were rejected as inconsistent with the IR observations [2]. Figure C shows that shells having a thickness > 5 km were capable of producing at least 3.9 GW of heat, but that shells thinner than 5 km were not.

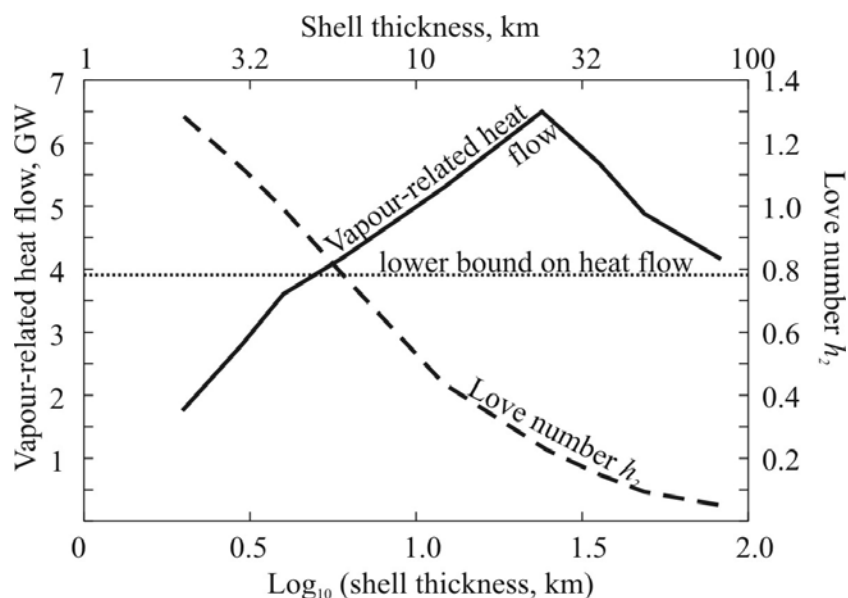


Figure C. Plot of Love number h_2 and heat flow (assuming 100% vapour recondensation and negligible conductive heating) as a function of ice shell thickness. Shear velocity u was derived assuming $u = 4 \times 10^{-5} h_2 \text{ ms}^{-1}$ (see text). Love numbers calculated assuming ice shell viscosity of 10^{13} Pa s and other parameters as given in caption to Figure 4; heat flow calculated using $\alpha=0.1$ and method and other parameters as given in caption to Figure 1.

Formatted: French (France)

4. Vapour Diffusion

The pore vapour diffusion equation

$$\partial \rho_v / \partial t = D \nabla^2 \rho_v + (1 - \alpha) H / L \phi$$

is derived using approaches similar to [20] and [21]. The source term due to volumetric heating $(1 - \alpha)H$ arises because heating within the solid ice results in an increase in the vapour density ρ_v in the interstitial pores, of volume fraction ϕ . The presence of the free parameter α is explained in Section 3 above. The Knudsen diffusivity D is calculated from [20] assuming $\phi=0.01$ and a pore radius of $56 \mu\text{m}$ (appropriate for a grain size of 1 mm). Vapour is allowed to escape into the brittle shear zone ($\rho_v=0$ boundary condition); other boundaries are impermeable ($d\rho_v/dx=0$). The equation is solved to steady-state. Figure D shows the steady-state vapour density distribution for the temperature distribution shown in Fig. 1; the right hand panel allows vapour escape via the brittle shear zone only, while the left hand panel also allows escape via the top surface. In steady state, vapour loss is balanced by vapour production due to shear heating. Therefore, the vapour fluxes in the two cases shown are almost identical--with minor differences arising because the latent heat is temperature-dependent [22]--and the results are independent of the porosity/permeability structure assumed. Results shown in the text all assume that vapour escapes via the brittle zone only.

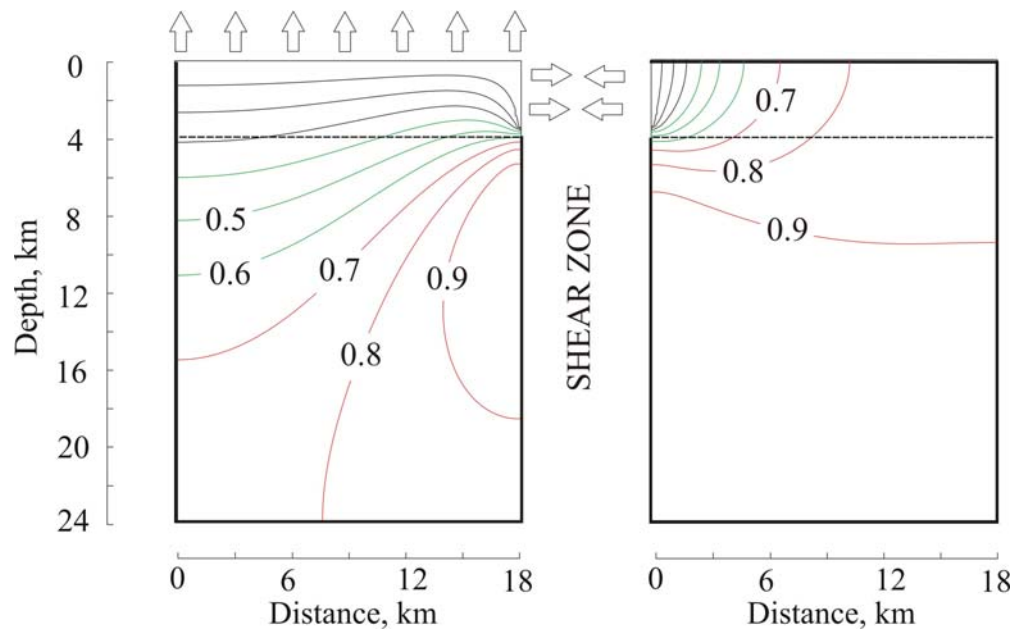


Figure D. Steady-state pore vapour density as a function of position for the situation shown in Fig. 1 and calculated using the methods described in the S.I. above. Density contours are normalized relative to the maximum pore vapour density present (5.6 and 11 kg m^{-3} for the left and right panels, respectively, where the porosity = 0.01). The two panels are identical except for the boundary conditions: left hand panel allows vapour (arrows) to escape from the top surface or laterally into the brittle shear zone; right panel allows vapour to escape into the brittle shear zone only. Solid lines denote impermeable boundaries. Vapour fluxes (4 kg s^{-1} per km length of shear zone) in both cases are almost identical because vapour loss is balanced by vapour production due to heating. In the left-hand panel only 45% of the total emitted vapour escapes via the shear zone.

Additional References

29. Murray, C.D. and S.F. Dermott, *Solar System Dynamics*, Cambridge Univ. Press (1999).
30. Ojakangas, G.W. and D.J. Stevenson, Thermal state of an ice shell on Europa, *Icarus* **81**, 220-241 (1989).

31. Mullen, M.E., Z. Crawford, R.T. Pappalardo, and J. Wahr, Visco-elastic surface stress on Europa. Proc. *Lunar Planet Sci. Conf.* XXXVII. Abstract #2350 (2006).
32. Wahr, J. M., The tidal motions of a rotating, elastic and oceanless Earth, PhD. Thesis, University of Colorado, Boulder (1979).
33. Turcotte, D.L. and G. Schubert, *Geodynamics*, Cambridge Univ. Press (2002).